Electronic Supplementary Information

Machine learning enabled electronic band-edge shapes and properties prediction of 2D transition metal dichalcogenide alloys

S1. Band structure comparison for six different atomic configurations simulated by *ab initio* method

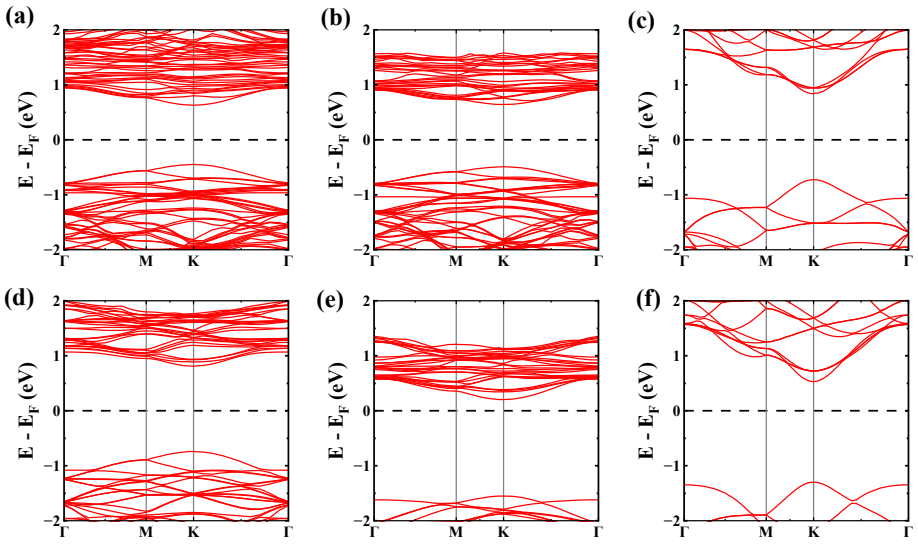

Fig. S1. Band structure comparison for six different atomic configurations simulated by *ab initio* method. The compositions $W_yMo_{1-y}X_2$ correspond to: (a) $y = 0.625$, X=Te, (b) $y = 0.1875$, X=Te, (c) $y = 1$, X=Se, (d) $y = 0..9375$, X=Se, (e) $y = 0.125$, X=S, (f) $y = 1$, X=S. The continuous and broken lines represent ground truth and ML predicted structures, respectively.

Figs. S1(a-f) show the DFT electronic band structures for $W_yMo_{1-y}X_2$ across Te, Se, and S chalcogenides with varying W content. An energy window of 4 eV centered on E_F was used to facilitate comparison. All compositions exhibited band gaps at the K point along the high-symmetry path $\Gamma \rightarrow M \rightarrow K \rightarrow \Gamma$. The Figs. S1(c) and (f) display fewer bands within this window because WSe_2 and WS_2 contain fewer atoms in the unit cell than the other compositions, resulting in a smaller number of allowed energy bands.

S2. Extra Trees Model Full Architecture

In Fig. S2 and S3, we can see the Extra trees structures for valence band and conduction band energy prediction, respectively. High level splits were basically based on k-points,which meant it was the most prominent feature in band energy prediction. Secondary splitting was based on other factors, such as Fermi energy, composition ratios, and lattice energy. We set the number of trees as 100 and maximum depth as *None*. Deeper structure in conduction band prediction model suggested higher variability in the conduction band. Deep/ highlighted nodesreferredd to extreme output value. The complex architecture effectively captured the nonlinear relationship between structural, electronic, and compositional features and the predicted band energies.

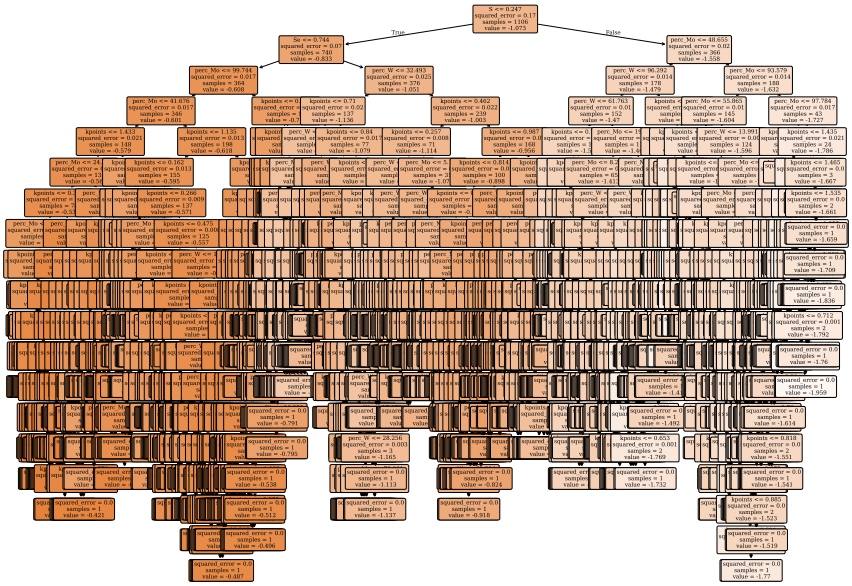

Fig. S2. Visualization of a single decision tree extracted from the Extra Trees model trained for valence band prediction.

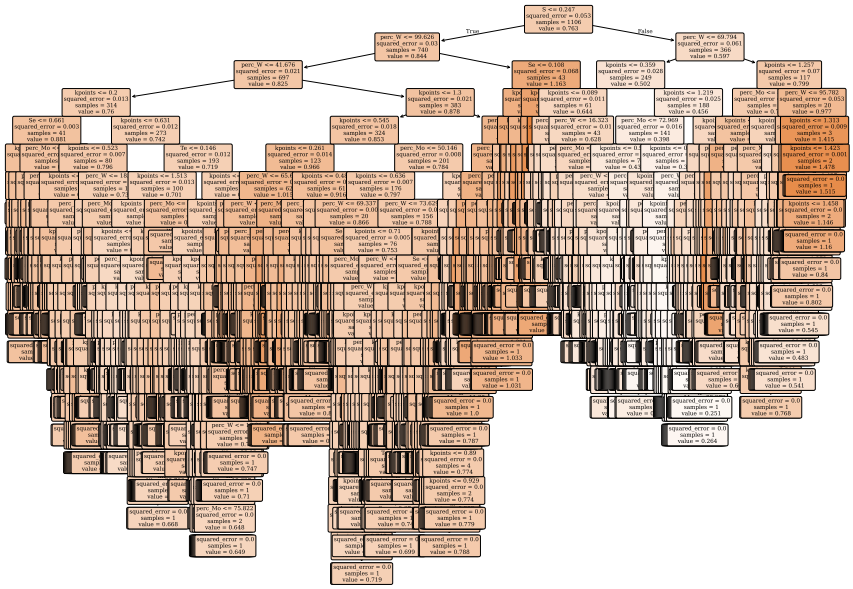

Fig. S3. Visualization of a single decision tree extracted from the Extra Trees model trained for conduction band prediction.

S3. Bandgap and Effective mass prediction

In this section, we presented the predicted band gap and effective carrier mass along with their deviation from the DFT calculated values. The dataset consisted of 51 different alloy compositions following the general formula $W_yMo_{1-y}X_2$. Results are summarised for X=Si in Table S1 and Fig. S4, X=Se in Table S2 and Fig. S5 and X=Te in Table S3 and Fig. S6. The prediction er-

ror for prediction remained significantly lower compared to that of effective mass calculation. This demonstrated the model's limitation in effective mass calculation despite its overall performanance remaining consistent. The sudden peaks observed in the plots corresponded to slightly higher error for some compositions, though the overall deviation is small.

Table S1. Comparison of bandgaps and effective masses calculated from DFT-simulated and Extra Trees (ET) predicted electronic band structures for varying compositions of $W_yMo_{1-y}S_2$

y	Bandgap (eV)			Effective mass (electron)			Effective mass (hole)		
	DFT	**ET**	**Error (%)**	**DFT**	**ET**	**Error (%)**	**DFT**	**ET**	**Error (%)**
1.0000	1.8281	1.8297	0.16	0.3721	0.4396	18.15	0.4992	0.5194	4.04
0.9375	1.8152	1.8207	0.30	1.4025	1.4640	4.39	1.8427	2.0460	11.03
0.8750	1.8069	1.8076	0.04	1.4724	1.5061	2.29	1.8917	1.9394	2.52
0.8125	1.8021	1.8069	0.27	1.5346	1.3734	10.50	1.9417	1.8762	3.38
0.7500	1.7751	1.7763	0.07	0.4810	0.5371	11.65	0.5407	0.5914	9.37
0.6875	1.7871	1.8050	1.00	1.6502	1.8728	13.49	2.0403	2.4266	18.94
0.6250	1.7821	1.7826	0.03	1.6957	1.5979	5.76	2.0787	2.0511	1.33
0.5625	1.7716	1.7779	0.36	1.7857	1.5474	13.35	2.1267	2.2462	5.62
0.5000	1.7466	1.7478	0.07	0.5228	0.6169	18.01	0.5810	0.6354	9.36
0.4375	1.7665	1.7665	0.00	1.8241	1.8622	2.09	2.2275	2.4715	10.95
0.3750	1.7635	1.7639	0.02	1.8814	1.9293	2.55	2.2714	2.2840	0.56
0.3125	1.7609	1.7640	0.18	1.9429	2.0796	7.04	2.3149	2.3983	3.60
0.2500	1.7342	1.7356	0.08	0.5591	0.6329	13.21	0.6211	0.6629	6.73
0.1875	1.7563	1.7563	0.00	1.9814	1.7378	12.30	2.3935	2.9708	24.12
0.1250	1.7535	1.7543	0.05	2.0076	1.9961	0.57	2.4242	2.4396	0.63
0.0625	1.7528	1.7572	0.25	2.0072	1.7781	11.41	2.4618	2.7070	9.96
0.0000	1.7510	1.7525	0.09	0.5595	0.5972	6.73	0.6612	0.7098	7.34

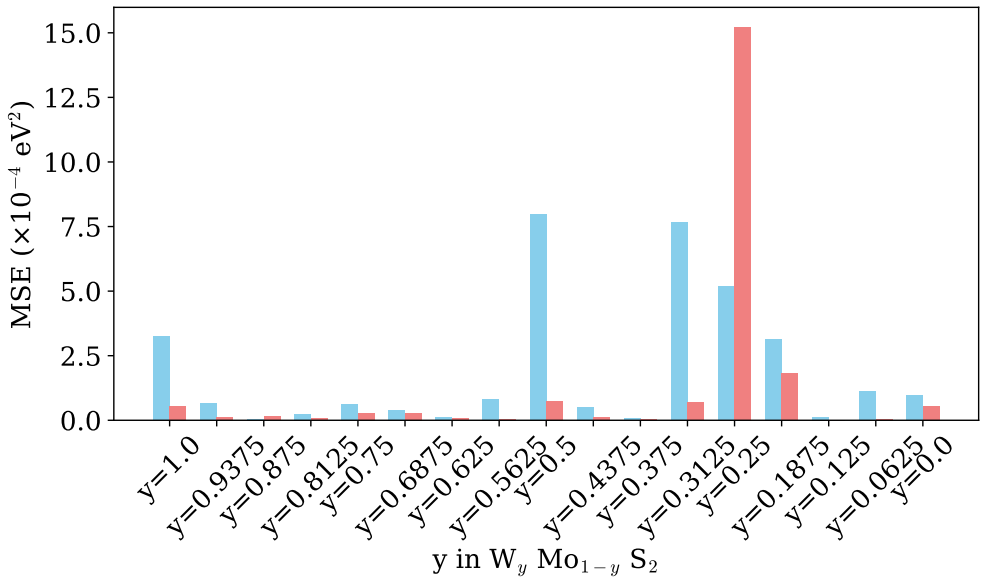

Fig. S4. Mean squared error (MSE) for conduction and valence band energy predictions across 17 different alloy compositions of form W_y Mo_{1-y} S_2 represented by blue and orange bars, respectively.

Table S2. Comparison of band gaps and effective masses calculated from DFT simulated and Extra Trees (ET) predicted electronic band structure for varying compositions of $W_yMo_{1-y}Se_2$

y	Bandgap (eV)			Effective mass (electron)			Effective mass (hole)		
	DFT	ET	Error (%)	DFT	ET	Error (%)	DFT	ET	Error (%)
1.0000	1.5641	1.5667	0.16	0.4709	0.5317	12.90	0.5818	0.6290	8.12
0.9375	1.5519	1.5569	0.32	1.7635	1.9443	10.25	2.1469	2.2822	6.30
0.8750	1.5460	1.5463	0.02	1.8777	2.0397	8.63	2.2068	2.3022	4.32
0.8125	1.5442	1.5445	0.02	1.9977	1.9911	0.33	2.2658	2.2224	1.92
0.7500	1.5124	1.5153	0.19	0.7285	0.8409	15.43	0.6364	0.7757	21.88
0.6875	1.5373	1.5378	0.04	2.1195	2.1716	2.46	2.3869	2.1319	10.68
0.6250	1.5291	1.5294	0.02	2.3157	2.3769	2.65	2.4495	2.3302	4.87
0.5625	1.5100	1.5122	0.15	2.4507	2.1455	12.45	2.4878	2.5984	4.45
0.5000	1.4884	1.4899	0.10	0.7880	0.8157	3.51	0.6943	0.8309	19.68
0.4375	1.5042	1.5044	0.01	2.5277	2.5533	1.01	2.6439	2.3541	10.96
0.3750	1.5080	1.5083	0.02	2.8172	2.9841	5.92	2.7082	2.7671	2.17
0.3125	1.5132	1.5245	0.74	2.6851	3.0342	13.00	2.7671	2.7864	0.70
0.2500	1.4796	1.4816	0.13	0.8046	0.9190	14.23	0.7543	0.8466	12.25
0.1875	1.5200	1.5176	0.16	2.6989	2.5836	4.27	2.8933	2.8645	1.00
0.1250	1.5177	1.5180	0.02	2.7245	2.7301	0.20	2.9438	2.8636	2.72
0.0625	1.5190	1.5193	0.02	2.7920	2.5561	8.45	2.9896	3.0657	2.54
0.0000	1.5218	1.5362	0.95	0.7961	0.9285	16.62	0.8169	0.9049	10.77

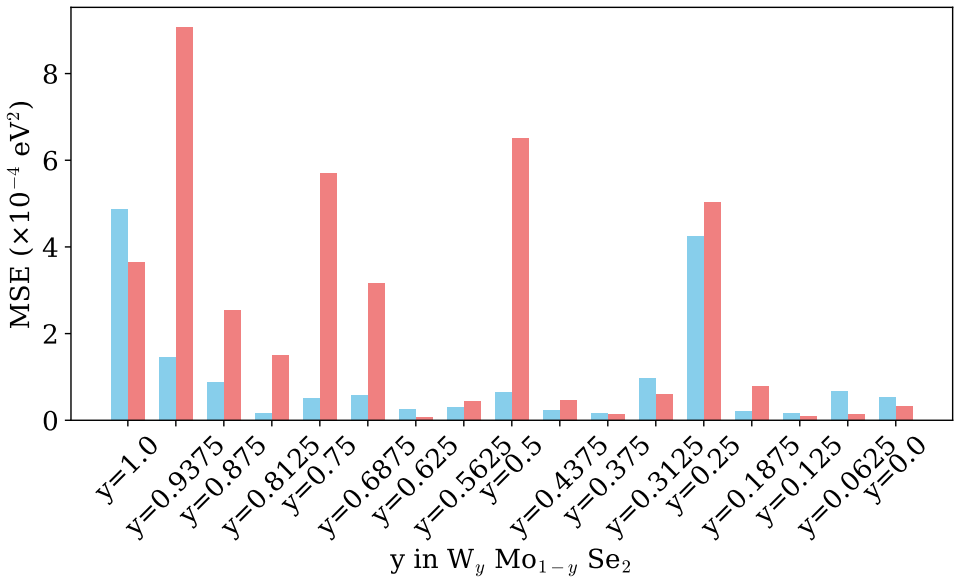

Fig. S5. Mean squared error (MSE) for conduction and valence band energy predictions across 17 different alloy compositions of form W_y Mo_{1-y} Se_2 represented by blue and orange bars, respectively.

Table S3. Comparison of band gaps and effective masses calculated from DFT simulated and Extra Trees (ET) predicted electronic band structure for varying compositions of $W_yMo_{1-y}Te_2$

y	Bandgap (eV)			Effective mass (electron)			Effective mass (hole)		
	DFT	ET	Error (%)	DFT	ET	Error (%)	DFT	ET	Error (%)
1.0000	1.0690	1.0713	0.21	0.4802	0.5124	6.69	0.6596	0.7065	7.12
0.9375	1.0728	1.0731	0.02	1.7896	1.9111	6.79	2.3538	2.0134	14.46
0.8750	1.0791	1.0795	0.04	1.8891	1.9809	4.86	2.4380	2.3932	1.84
0.8125	1.0872	1.0910	0.35	1.9817	1.9236	2.93	2.5236	2.5219	0.07
0.7500	1.0882	1.1059	1.63	0.6243	0.8073	29.31	0.7384	1.0468	41.78
0.6875	1.0989	1.0993	0.04	2.1736	1.8085	16.80	2.6961	2.0382	24.40
0.6250	1.1039	1.1046	0.06	2.2264	2.2935	3.01	2.7937	2.4343	12.87
0.5625	1.1040	1.1040	0.00	2.3741	2.3311	1.81	2.8874	2.8350	1.81
0.5000	1.1010	1.1021	0.10	0.7882	0.8191	3.93	0.8267	0.8925	7.96
0.4375	1.1139	1.1141	0.02	2.6621	2.6108	1.93	3.0766	3.0651	0.37
0.3750	1.1198	1.1223	0.22	2.7879	2.8183	1.09	3.1732	3.3193	4.60
0.3125	1.1229	1.1232	0.02	3.0502	3.1209	2.32	3.2550	3.2578	0.09
0.2500	1.1134	1.1148	0.13	0.9547	1.2373	29.60	0.9186	1.1860	29.11
0.1875	1.1330	1.1280	0.44	3.0021	2.5703	14.38	3.4482	3.3014	4.26
0.1250	1.1398	1.1363	0.31	3.1443	3.0809	2.01	3.5722	4.0117	12.30
0.0625	1.1448	1.1431	0.15	3.2464	3.0113	7.24	3.6770	4.2531	15.67
0.0000	1.1474	1.1578	0.91	1.0994	1.3714	24.74	1.0231	1.2968	26.75

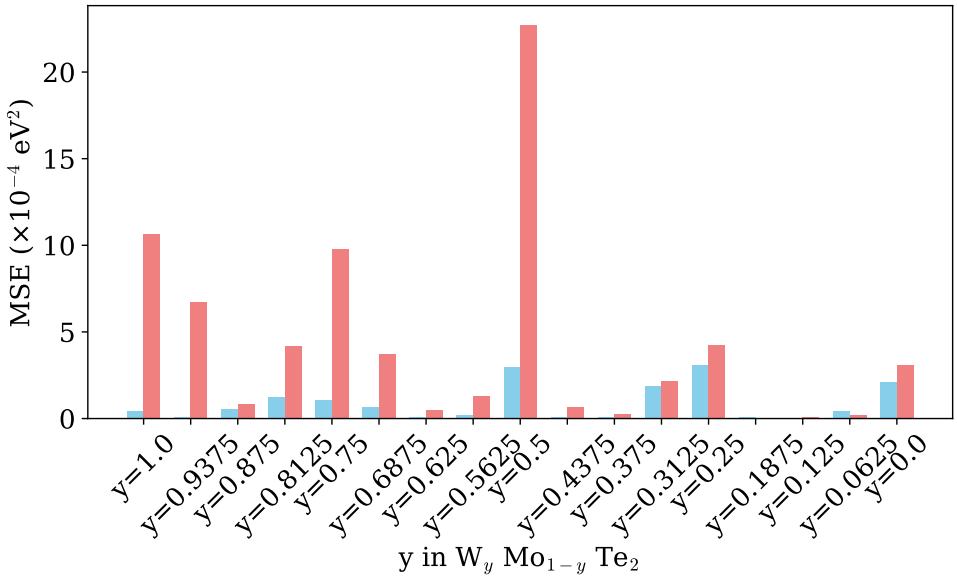

Fig. S6. Mean squared error (MSE) for conduction and valence band energy predictions across 17 different alloy compositions of form W_y Mo_{1-y} Te_2 represented by blue and orange bars, respectively.

S4. Effect of Different Supercell Sizes on Electronic Band Dispersion

Table S4. Supercell size, band gap, and effective mass for electron and hole of pristine WS_2

Supercell size	Band gap (eV)	Effective mass of electron	Effective mass of hole
$1 \times 1 \times 1$	1.82	0.33 m_o	0.46 m_o
$2 \times 2 \times 1$	1.83	0.37 m_o	0.52 m_o
$3 \times 3 \times 1$	1.83	0.35 m_o	0.51 m_o
$4 \times 4 \times 1$	1.83	0.37 m_o	0.51 m_o

To examine the sensitivity of the band dispersion and the electron and hole effective masses to the supercell size, we calculated the band structures and extracted parabolic effective masses for pristine WS_2 using the unit cell $(1 \times 1 \times 1)$, $(2 \times 2 \times 1)$, and $(3 \times 3 \times 1)$ supercells (corresponding to WS_2 and W_4S_8, and W_9S_{18}) in addition to $(4 \times 4 \times 1)$ supercell ($W_{16}S_{32}$). We found almost identical band gaps ($\sim$ 1.83 eV) in all cases, with a minor discrepancy in the effective masses of the hole and electron in larger supercells. In the unit cell, electron and hole effective masses were 0.33 m_o and 0.46 m_o, respectively, whereas for the $(2 \times 2 \times 1)$ supercell, they were 0.37 m_o and 0.52 m_o, respectively, and for the $(3 \times 3 \times 1)$ supercell, they were 0.35 m_o and 0.51 m_o, respectively. We found that, for larger supercells, the effective masses were similar. Table. S4 reports band gaps and effective masses for four different supercells of WS_2, including $(1 \times 1 \times 1)$, $(2 \times 2 \times 1)$, $(3 \times 3 \times 1)$, and $(4 \times 4 \times 1)$.

S5. k-grid Convergence Test

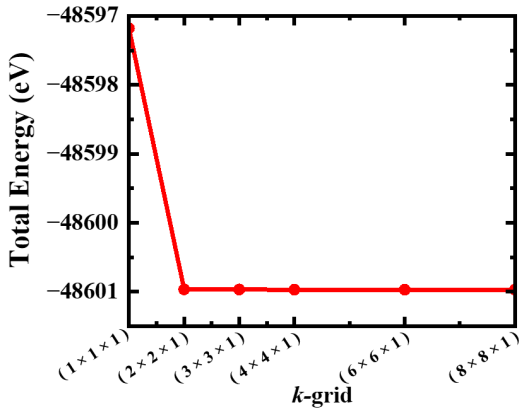

Fig. S7. Total energy (eV) variation with respect to different k-grid sizes of WS_2

To verify convergence for the present $(4 \times 4 \times 1)$ supercell, we computed the self-consistent total energy using Monkhorst–Pack k meshes of $(1 \times 1 \times 1)$, $(2 \times 2 \times 1)$, $(3 \times 3 \times 1)$, $(4 \times 4 \times 1)$, $(6 \times 6 \times 1)$, and $(8 \times 8 \times 1)$. As shown in Fig. S7, the total-energy variation of pristine WS_2 is minimal after $(2 \times 2 \times 1)$ k-grid size, indicating that the selected k-point density was sufficiently converged while keeping the computational cost manageable. Since a larger real-space supercell corresponds to a smaller reciprocal-space Brillouin zone, a reduced k-point mesh is typically sufficient for supercell calculations. This is consistent with prior analyses of Brillouin-zone sampling in supercell-based calculations, where the number of k-points can be decreased as the supercell size is increased [1].

References

1. G. Makov, R. Shah, and M. Payne, "Periodic boundary conditions in ab initio calculations. ii. brillouin-zone sampling for aperiodic systems," Phys. Rev. B **53**, 15513 (1996).